

# On the Cause of the 1930s Dust Bowl

Siegfried D. Schubert,<sup>1\*</sup> Max J. Suarez,<sup>1</sup> Philip J. Pegion,<sup>1,2</sup>  
Randal D. Koster,<sup>1</sup> Julio T. Bacmeister<sup>1,3</sup>

During the 1930s, the United States experienced one of the most devastating droughts of the past century. The drought affected almost two-thirds of the country and parts of Mexico and Canada and was infamous for the numerous dust storms that occurred in the southern Great Plains. In this study, we present model results that indicate that the drought was caused by anomalous tropical sea surface temperatures during that decade and that interactions between the atmosphere and the land surface increased its severity. We also contrast the 1930s drought with other North American droughts of the 20th century.

In the United States, the 1930s were characterized by a decade of rainfall deficits and high temperatures that desiccated much of the land surface of the Great Plains. The drought and its associated dust storms created one of the most severe environmental catastrophes in U.S. history and led to the popular characterization of much of the southern Great Plains as the “Dust Bowl” (1, 2).

While progress has been made in understanding some of the important processes contributing to drought conditions (3–7), the mechanisms by which a drought can be maintained over many years are not well established. A number of studies have used the historical record of meteorological and oceanographic observations to identify statistical relations between slowly varying Pacific Ocean sea surface temperatures (SSTs) and precipitation over the Great Plains (8, 9). The record of observations, however, is too short to provide definitive results for long-term drought. Understanding the causes of the 1930s drought is particularly challenging in view of the scarcity of upper-air meteorological observations prior to about 1950.

Several recent studies using state-of-the-art atmospheric general circulation models (AGCMs) have shown how SST anomalies can produce prolonged drought conditions. Tropical SST anomalies, in particular, were found to contribute to recent prolonged drought conditions over much of the northern middle latitudes (10), to drought in the Great Plains (11), and to

drought conditions in the African Sahel region during the 1970s and 1980s (12).

The importance of the Pacific SSTs (the pan-Pacific pattern) in forcing long-term precipitation variations in the Great Plains led us to expect that this pattern would be an important factor during the Dust Bowl when drought was most severe. SST anomalies, however, were surprisingly weak throughout the tropical Pacific during the 1930s. This prompted a much closer look at the relationship between SST anomalies and the generation of the Dust Bowl.

Our study is based on a number of century-long simulations carried out with the NASA Seasonal-to-Interannual Prediction Project (NSIPP) atmospheric general circulation model (13), the same model used in (11) and (12), although run here at a somewhat coarser horizontal resolution (14). The basic model simulations are an ensemble of fourteen 100-year (1902 to 2001) runs forced by observed monthly SSTs (15). These simulations will be referred to as the C20C runs, because they were carried out as part of the Climate of the 20th Century project (16). The runs differ only in their initial atmospheric conditions. As such, the degree of similarity in the runs (the “signal”) provides us with an assessment of how much the SSTs control Great Plains climate variations, while the disagreement among the runs (the “noise”) provides us with an estimate of the unpredictable component of the climate variability.

Figure 1 shows time series of the precipitation averaged over the Great Plains and filtered to retain time scales longer than about 6 years, using data from observations (17) and from the 14 simulations. The time series of the observed and simulated anomalies show considerable variability, with extended periods of both above- and below-normal conditions throughout the century.

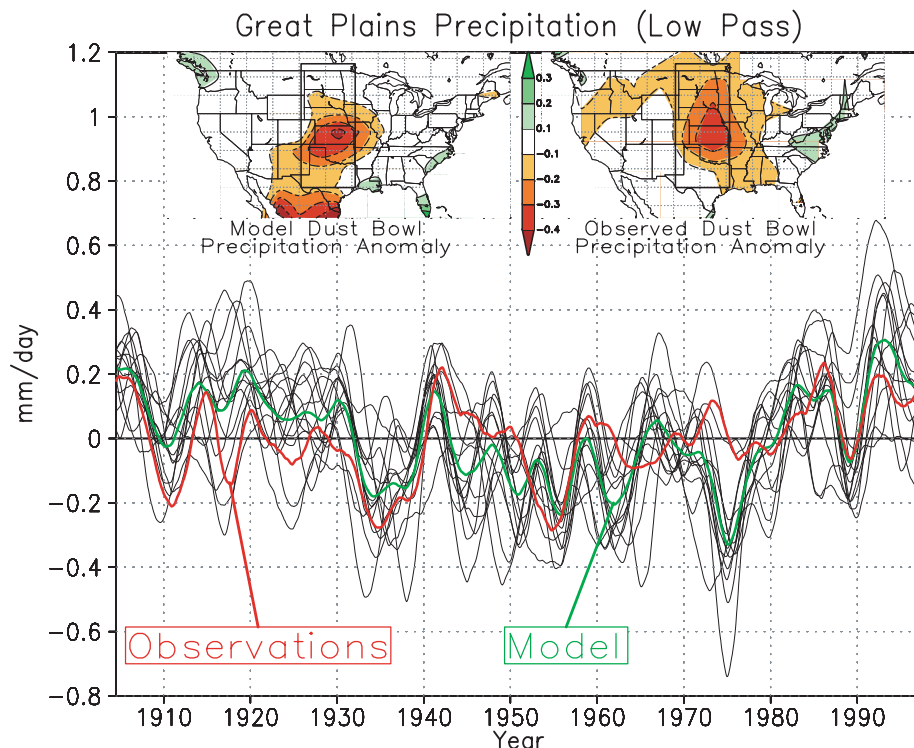


**Fig. 1.** Time series of precipitation anomalies averaged over the U.S. Great Plains region (30°N to 50°N, 95°W to 105°W; see box in insets). A filter (28) is applied to remove time scales shorter than about 6 years. The thin black curves are the results from the 14 ensemble members from the C20C runs. The green solid curve is the ensemble mean. The red curve shows the observations. The maps show the simulated (left) and observed (right) precipitation anomalies averaged over the Dust Bowl period (1932 to 1938). Units, mm/day.

<sup>1</sup>Earth Sciences Directorate, National Aeronautics and Space Administration/Goddard Space Flight Center, Greenbelt, Maryland 20771, USA. <sup>2</sup>Science Applications International Corporation, Beltsville, Maryland 20705, USA. <sup>3</sup>Goddard Earth Sciences and Technology Center (GEST), University of Maryland, Baltimore, MD 21250, USA.

\*To whom correspondence should be addressed: E-mail: schubert@gmao.gsfc.nasa.gov

REPORTS

The correlation between the observed and ensemble mean anomalies is 0.57. The correlation between the ensemble mean and the individual simulations, a measure of the highest correlation we can expect with the observations, ranges from 0.53 to 0.79. While there is considerable scatter among

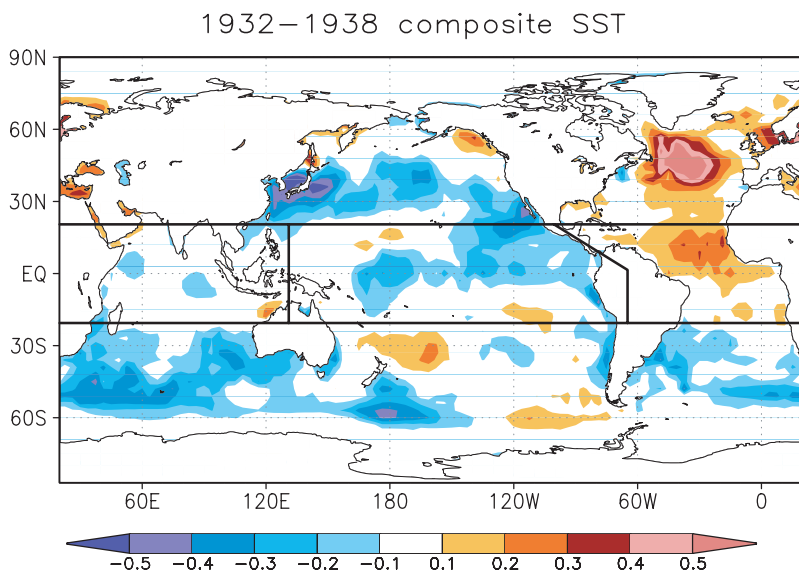
the ensemble members, there are periods during which all the curves tend to follow one another. In particular, during the 1930s almost all of the runs show a tendency for dry conditions, consistent with the observations. The dry conditions of the 1930s are followed, in the early 1940s, by a rapid

transition by all ensemble members to wetter conditions, again consistent with the observations. In general, the simulations agree with the observations to the extent that the observed anomalies fall within the scatter of the ensemble members.

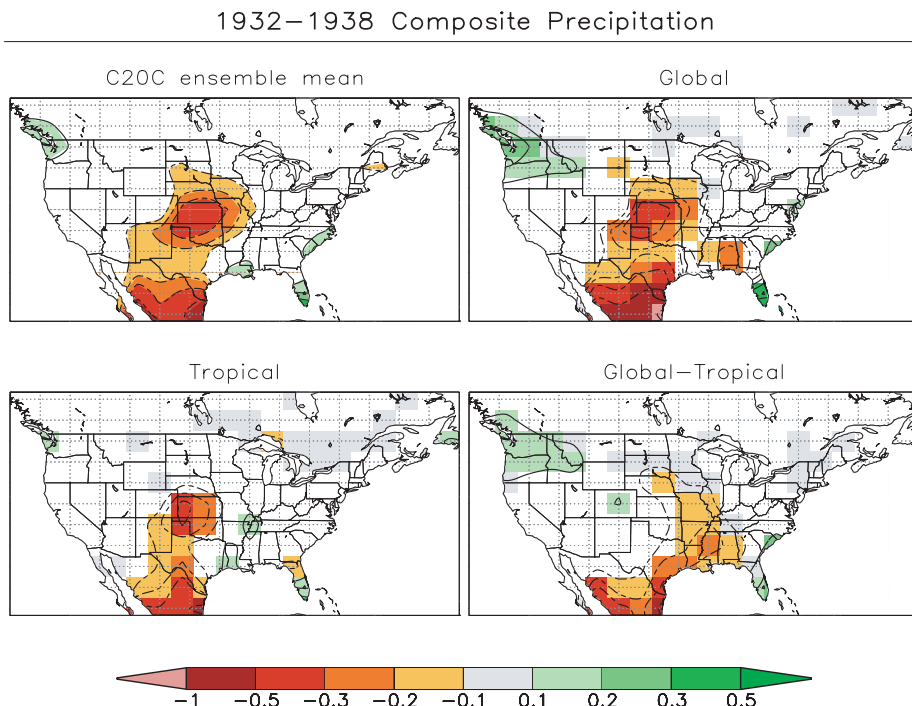
Figure 1 includes maps of the ensemble mean and observed precipitation anomalies averaged over the Dust Bowl period (1932 to 1938). The observations show deficits exceeding 0.1 mm/day covering much of the central United States, with peak deficits exceeding 0.3 mm/day centered on Kansas. The simulated anomalies are similar to the observed, with peak deficits of similar magnitude and again centered over Kansas. The main discrepancy is the large deficit simulated over Mexico that does not occur in the observations (18). The simulation also fails to capture the full spatial extent of the drought, particularly the dry conditions that were observed over the northern Great Plains and parts of Canada. An inspection of the individual ensemble members shows that this discrepancy occurs as a result of the ensemble averaging, which acts to filter out the unpredictable (noise) component of the simulated anomalies. In fact, there is wide variability in the spatial pattern of the dry conditions among the ensemble members, with some showing negative precipitation anomalies ( $< -0.1$ ) extending well into Canada and covering an area that exceeds that of the observed anomalies.

Figure 1 also reveals some rather peculiar model behavior during the mid-1970s. While the observations and 2 of the ensemble members show a tendency for slightly wet or neutral conditions, 12 of the ensemble members predict a drought even more severe than that during the 1930s. This highlights the probabilistic nature of the drought prediction problem and suggests, if we believe the model results, that the central United States was lucky to have had near normal conditions during the 1970s, because the probability of having a major drought was rather high (12 chances out of 14). In fact, the historical tendency for droughts to occur in the Great Plains roughly every 20 years (1910s, 1930s, and 1950s), together with the very dry conditions that existed over parts of the central United States by the mid-1970s, collectively led to speculation at the time that we were about to enter an extended dry period (19, 20).

Figure 2 shows our best estimate of the global SST anomalies (15, 21) that occurred during the Dust Bowl period. It must be emphasized that this time-averaged field is based on extrapolations of a rather limited number of ship observations using empirical orthogonal functions. Figure 2 shows that the anomalies are negative in most places, including the tropical Pacific and North Pacific, as well as much of the Southern Ocean. Positive anomalies occur in the tropical and



**Fig. 2.** The global SST anomalies averaged for the Dust Bowl period (1932 to 1938). The boxes delineate the various subregions (tropical oceans, Indian Ocean, Pacific Ocean, Atlantic Ocean) used in designing the idealized SST forcing experiments. The anomalies are the differences from the 1902 to 1999 SST climatology (15). Units, °C.



**Fig. 3.** (Top left) Ensemble mean precipitation anomalies averaged for the period 1932 to 1938 from the C20C runs. (Top right) The 100-year mean precipitation anomalies from the Global SST run (Fig. 2 and Table 1). (Bottom left) Same as the top right panel except for the Tropical SST run. (Bottom right) The difference between the precipitation anomalies from the Global SST and the Tropical SST runs. Units, mm/day. In all but the C20C panel, values are shaded only if they are significant at the 10% level based on a  $t$  test. The contour intervals are the same as the shading intervals (see color bar), with dashed contours indicating negative values.

North Atlantic Oceans and in some regions of the South Pacific. Surprisingly, the tropical anomalies tend to be small, generally less than 0.3°C. The largest anomalies occur in the North Atlantic and just off the coast of Asia, where they exceed 0.5°C.

To understand the importance of each of these features to the 1930s drought, we carried out a number of idealized experiments in which SST anomalies, averaged over the 1932 to 1938 Dust Bowl period, were applied only to particular subregions (see outlines in Fig. 2). The remainder of the ocean was assigned climatological SSTs. Table 1 summarizes the experiments. Our aim was to separate the contributions to the drought from each of the three tropical basins (Indian, Pacific and Atlantic) and the extratropics (22).

We first examined whether forcing the model with the 1932 to 1938 time-mean SST anomalies produces the same time mean response in the Great Plains precipitation as that obtained in the original C20C ensemble. The top two panels of Fig. 3 compare the ensemble mean precipitation anomalies from the C20C runs averaged from 1932 to 1938 with those from the Global run. The results are quite similar. In addition to the dry anomalies, the idealized forcing also reproduces some of the wet anomalies in the Pacific Northwest and along the southeast coast. There are some discrepancies between the runs. Most notably, the rainfall deficits that extend into Alabama in the Global run are absent in the C20C runs. Despite such minor differences, which must be artifacts of the Global run, it appears that the basic drought conditions simulated by the model in the Great Plains during the 1930s can be explained as a response to the time-mean global SST anomalies and that the year-to-year variations of the SSTs in that decade played at most a secondary role in shaping the drought.

We next tried to distinguish between tropical and extratropical effects. The results of the tropical run (lower left panel of Fig. 3) show that the main features of the drought are reproduced with the tropical SST forcing alone. The Global-minus-Tropical difference map (lower right panel) shows that the impact of the extratropical SSTs is much smaller. Extratropical anomalies tend to broaden the region of drought conditions, especially to the east and south of the central Great Plains. They also increase the region of wet anomalies in the Pacific Northwest.

The precipitation anomalies from the different model runs, including the contributions from the different tropical basins and the extratropics, averaged over the core Dust Bowl region (the rectangles in Fig. 4) are shown in fig. S1. The results show that the contributions from the tropical Pacific

and tropical Atlantic are significant, while those from the tropical Indian Ocean and the extratropics are not (22). Figure S1 also shows the results of repeating the Global run, but in this case disabling the interactions between the atmosphere and land surface [the Fixed Beta run(22)]. Preventing this feedback reduces the precipitation deficit by 50%. Thus, land-atmosphere interaction appears to be responsible for much of the drought severity. The much tighter confidence intervals associated with the Fixed Beta results (fig. S1) show that without soil moisture feedbacks, precipitation variability is greatly reduced, consistent with previous studies employing the same model (7, 11). The spatial distribution of the precipitation

anomalies from the Fixed Beta run shows that the reduced deficits span the Great Plains (Fig. 4). These results are consistent with previous work (7) showing that the Great Plains region is particularly sensitive to soil moisture changes.

The results presented so far have been for annual-mean conditions. It is well known, however, that most of the rain in the Great Plains tends to fall during the spring and summer seasons. We show in Fig. 5 the seasonal distribution of the area-averaged precipitation anomalies from observations, the Global run, and the Fixed Beta run. The results from the Global run are quite similar to the observed (23), though there is a general tendency to underestimate the deficits. The largest deficits

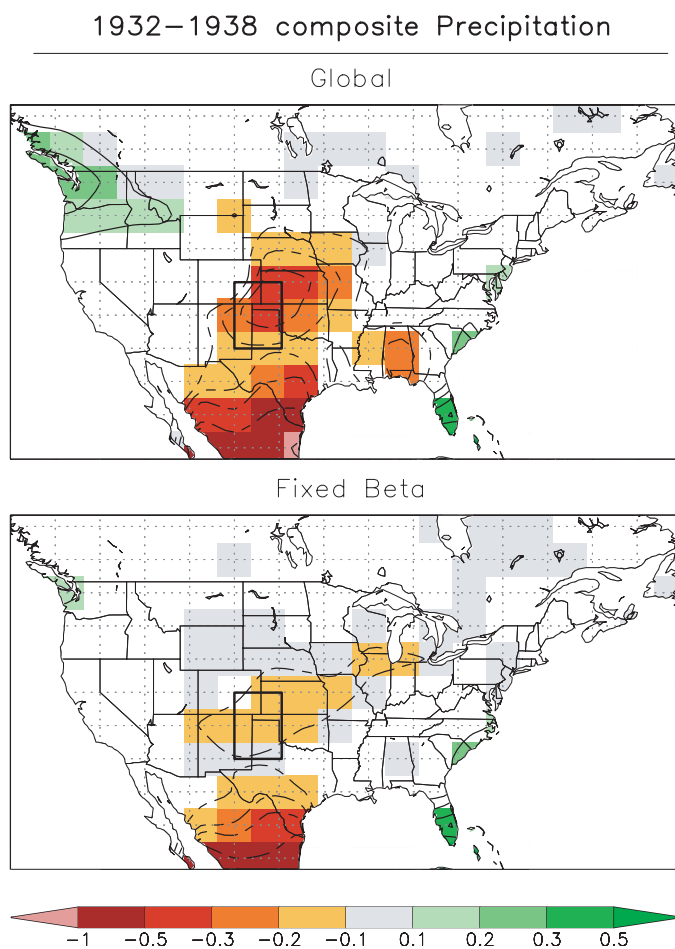
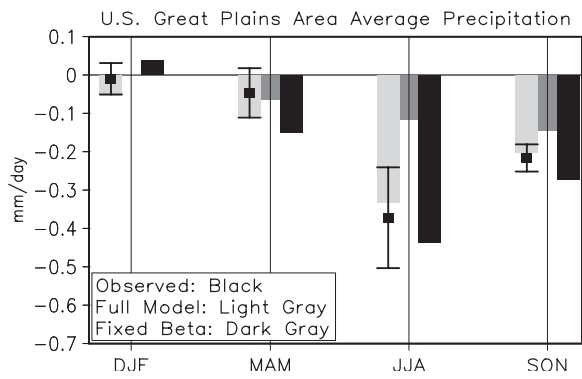


**Fig. 4. (Top)** Mean precipitation anomalies from the Global SST run. **(Bottom)** Mean precipitation anomalies from the Fixed Beta run. Shading indicates significance at the 10% level based on a *t* test. The contour intervals are the same as the shading intervals (see color bar), with dashed contours indicating negative values. The boxes indicate the core Dust Bowl region (36°N to 39°N, 99.5°W to 105°W). Units, mm/day.

**Table 1.** The idealized SST experiments. The anomalies are the time-averaged (1932 to 1938) deviations from the 1902 to 1999 mean (22). All runs are 100 years in length. The regions are defined in Fig. 2.

Run	SST
Control	Climatological (average of 1902 to 1999)
Global	Global anomalies
Tropical	Anomalies confined to tropics, climatological elsewhere
Pacific	Anomalies confined to tropical Pacific
PacAtl	Anomalies confined to tropical Pacific and tropical Atlantic
PaInd	Anomalies confined to tropical Pacific and tropical Indian Ocean
Fixed Beta	Global anomalies and atmosphere-land surface interaction disabled

**Fig. 5.** The seasonal variation of the mean precipitation anomalies averaged over the U.S. Great Plains (see box in insets in Fig. 1). The black bars show the observed values averaged over the Dust Bowl period (1932 to 1938). The light gray bars are the 100-year averaged results from the Global SST run. The dark gray bars are the 100-year averaged results from the Fixed Beta run. The small boxes and associated thin bars show the ensemble mean and 90% confidence intervals, respectively, of the 1932 to 1938 precipitation anomalies from the C20C runs. The labels on the abscissa indicate the seasons, where DJF is December, January, February; MAM is March, April, May; JJA is June, July, August; SON is September, October, November. Note that for DJF, the Fixed Beta run produces anomalies that are too small to show up in the figure.



occur during the warm season, with about half the deficit occurring during the summer months. Somewhat surprisingly, the fall season has larger deficits than the spring season. The winter season precipitation anomalies are by comparison rather small; in fact, the observed winter anomaly is slightly positive. The main impact of disabling the interactions with the land surface is to reduce dramatically the deficit during the summer. Figure 5 includes the ensemble mean and 90% confidence intervals of the precipitation anomalies from the C20C runs. Comparing those results with those from the Global run provides further evidence that the Global run reproduces the basic features of the C20C run—in this case, the annual cycle of the anomalies. The fact that the confidence intervals for the C20C anomalies encompass zero for winter and spring confirms that the significant precipitation anomalies for the core region are confined to the summer and fall season.

These results suggest that we must look to the summer and fall seasons to understand the mechanisms linking tropical SST anomalies to the Dust Bowl region (24). An analysis of the summer circulation changes (not shown) suggests that the role of the cold Pacific SST anomalies was to generate a global-scale response in the upper troposphere (negative height anomalies in the tropics and a tendency for positive height anomalies in the middle latitudes) that suppressed rainfall over the Great Plains. The warm Atlantic SST anomalies produced two upper-level anticyclonic circulation anomalies on either side of the equator, with the northern anomaly extending across the Gulf of Mexico and the southern United States. In the lower troposphere, the response to the warm Atlantic SST anomalies was a cyclonic circulation anomaly positioned to suppress the supply of moisture entering the continent from the Gulf of Mex-

ico. It is noteworthy that the Atlantic response is confined almost exclusively to the summer and fall season.

While the severity, extent, and duration of the 1930s drought was unusual for the 20th century, proxy climate records indicate that major droughts have occurred in the Great Plains approximately once or twice a century over the past 400 years (25). There is evidence for multidecadal droughts during the late 13th and 16th centuries that were of much greater severity and duration than those of the 20th century (25). For example, tree-ring analyses in Nebraska suggest that the drought that began in the late 13th century lasted 38 years (26). An analysis of the other major central U.S. droughts of the 20th century (11) suggests that a cool tropical Pacific is common to all. Only the Dust Bowl drought, however, combined cool Pacific SSTs with a warm Atlantic Ocean. Figure 1 shows that since the early 1980s (with the exception of 1987 to 1989), the Great Plains generally experienced above-normal precipitation. On the other hand, much of the western (especially the southwestern) United States, including some parts of the Great Plains, experienced below-normal precipitation during the past 5 years, leading to moderate or extreme drought conditions (27). The cause of this most recent drought is unclear, although a preliminary look at the relation between SSTs and long-term precipitation variations over the southwestern United States from our C20C runs suggests a strong link to the pan-Pacific pattern discussed earlier. One difference compared with the Great Plains is that the southwestern United States appears to have a stronger link to the Indian Ocean SSTs.

**References and Notes**

1. D. Worster, *Dust Bowl: The Southern Great Plains in the 1930s* (Oxford University Press, New York, 1979).
2. The "Dust Bowl" was loosely defined to be the region

encompassing the western third of Kansas, southeastern Colorado, the Oklahoma Panhandle, the northern two-thirds of the Texas Panhandle, and northeastern New Mexico.

3. J. Namias, *Mon. Weather Rev.* **83**, 199 (1955).
4. K. E. Trenberth, G. W. Branstator, P. A. Arkin, *Science* **242**, 1640 (1988).
5. R. Atlas, N. Wolfson, J. Terry, *J. Clim.* **6**, 2034 (1993).
6. K. C. Mo, J. Nogues-Paegle, R. W. Higgins, *J. Clim.* **10**, 3028 (1997).
7. R. D. Koster, M. J. Suarez, M. Heiser, *J. Hydrometeorol* **1**, 26 (2000).
8. M. Ting, H. Wang, *J. Clim.* **10**, 1853 (1997).
9. M. Barlow, S. Nigam, E. H. Berbery, *J. Clim.* **14**, 2105 (2001).
10. M. P. Hoerling, A. Kumar, *Science* **299**, 691 (2003).
11. S. D. Schubert, M. J. Suarez, P. J. Pegion, R. D. Koster, J. T. Bacmeister, *J. Clim.* **17**, 485 (2004).
12. A. Giannini, R. Saravanan, P. Chang, *Science* **302**, 1027 (2003).
13. J. Bacmeister, P. J. Pegion, S. D. Schubert, M. J. Suarez, "An atlas of seasonal means simulated by the NSIPP 1 atmospheric GCM" (NASA Tech. Memo. No. 104606, volume 17, Goddard Space Flight Center, Greenbelt, MD, 2000).
14. The model was run with a 3° latitude by 3.75° longitude horizontal grid as compared with the 2° latitude by 2.5° longitude grid used in the earlier study (17). The resolution change was made for computational efficiency and does not appear to have much impact on the model's basic climatology or its variability.
15. N. A. Rayner, *et al.*, *J. Geophys. Res.* **108**, 4407 (2003).
16. C. Folland, J. Shukla, J. Hiner, M. Rodwell, in *CLIVAR Exchanges*, vol. 7, no. 2 (June 2002), pp. 37–39.
17. R. Vose *et al.*, "The global historical climatology network: long-term monthly temperature, precipitation, sea level pressure, and station pressure data" (ORNL/CDIAC-53, NDP-041. Carbon Dioxide Information Analysis Center, Oak Ridge National Laboratory, Oak Ridge, Tennessee, 1992).
18. Mexico experienced somewhat above-normal precipitation during the 1930s. This may have been due, in part, to a number of hurricanes that made landfall over Mexico, especially during 1933 and 1936. The coarse resolution of the model runs precludes the simulation of hurricanes; this may account for some of the unrealistic dry conditions simulated by the model over Mexico.
19. J. R. Borchert, *Ann. Assoc. Am. Geogr.* **61**, 1 (1971).
20. N. J. Rosenberg, in *North American Droughts*, N. J. Rosenberg, Ed. (AAAS Selected Symposia Series, Westview Press, Boulder Colorado, 1978), pp. 1–7.
21. The SST anomalies used to force the model were computed separately for each calendar month as the sum of a mean annual cycle (computed for the period 1902 to 1999) and the SST anomaly field for that calendar month. In Fig. 2, we show only the time-averaged anomalies.
22. Materials and methods are available as supporting material on *Science Online*.
23. It should be noted that current AGCMs (including this model) tend to have difficulty simulating warm-season continental rainfall. In the Great Plains, this is primarily due to a poor representation of nighttime precipitation and appears to be strongly tied to deficiencies in how the models represent convective rain. The good comparison with observations shown in Fig. 5 indicates that despite any such deficiencies in the warm season precipitation climatology, the NSIPP model produces a realistic annual cycle in the response to the SST forcing.
24. It can be argued that precipitation deficits during summer are the result of anomalies that are "remembered" from the previous spring and winter. In these calculations, any such memory of the previous season's condition would come from the land surface. The Fixed Beta run suggests, that at most, such an impact would account for 50% of the summer precipitation deficit. Furthermore, the lack of substantial ensemble mean precipitation deficits

over the continental United States during the spring and winter seasons (not shown) suggests that the impact of the land is primarily a contemporaneous feedback and not the result of memory of the previous season's anomalies. We note that the observations do show substantial precipitation deficits to the north and east of the core region during spring, but similar anomalies are also obtained for some of the individual model runs, suggesting that the observed precipitation anomalies in the spring may not have been forced by SST anomalies.

25. C. A. Woodhouse, J. T. Overpeck, *Bull. Am. Meteorol. Soc.* **79**, 2693 (1998).
26. D. L. Bark, in *North American Droughts*, N. J. Rosenberg, Ed. (AAAS Selected Symposia Series, Westview Press, Boulder Colorado, 1978), pp. 9–23.
27. U.S. Drought Monitoring Page ([www.drought.unl.edu/dm/monitor.html](http://www.drought.unl.edu/dm/monitor.html)).
28. Y. Zhang, J. M. Wallace, D. Battisti, *J. Clim.* **10**, 1004 (1997).
29. This work was supported by the NASA Earth Science

Enterprise's Global Modeling and Analysis Program and the NASA Seasonal-to-Interannual Prediction Project.

#### Supporting Online Material

[www.sciencemag.org/cgi/content/full/303/5665/1855/DC1](http://www.sciencemag.org/cgi/content/full/303/5665/1855/DC1)

Materials and Methods

Fig. S1

References and Notes

23 December 2003; accepted 20 February 2004

# Laboratory Earthquakes: The Sub-Rayleigh-to-Supershear Rupture Transition

Kaiwen Xia,<sup>1,2</sup> Ares J. Rosakis,<sup>2</sup> Hiroo Kanamori<sup>1\*</sup>

We report on the experimental observation of spontaneously nucleated supershear rupture and on the visualization of sub-Rayleigh-to-supershear rupture transitions in frictionally held interfaces. The laboratory experiments mimic natural earthquakes. The results suggest that under certain conditions supershear rupture propagation can be facilitated during large earthquake events.

The surface-wave magnitude ( $M_s$ ) 8.1 ( $M_w$  7.8) central Kunlunshan earthquake that occurred on 14 November 2001 was an extraordinary event from the point of view of dynamic rupture mechanics. The rupture occurred over a long, near-vertical, strike-slip fault segment of the active Kunlunshan fault and featured an exceptionally long (400 km) surface rupture zone and large surface slip displacements (1). Modeling of the rupture speed history (2) suggests rupture speeds that are slower than the Rayleigh wave speed,  $c_R$ , for the first 100 km, transitioning to supershear (speed higher than the shear wave speed,  $c_s$ ) for the remaining 300 km of rupture growth. Other events, such as the 1979 Imperial Valley earthquake (3, 4), the 1992 Landers earthquake (5), the 1999 Izmit earthquake (6), and the 2002 Denali earthquake (7), may also have featured supershear speeds. Supershear was also predicted theoretically (8, 9) and numerically (10, 11). Even with these estimates and predictions at hand, the question of whether natural earthquake ruptures can propagate at supershear speeds is still a subject of active debate. In addition, the exact mechanism for transition of a spontaneously nucleated rupture from sub-Rayleigh to supershear rupture speed is not clear. One answer to this question was provided by the two-dimensional Burridge-

Andrews mechanism (BAM) (10). Recent numerical investigations of frictional rupture have suggested alternative, asperity-based, three-dimensional mechanisms (12–14). Whether and how supershear rupture occurs during earthquakes has important implications for seismic hazards, because the rupture speed influences the character of near-field ground motions.

To answer the above-stated questions, we conducted experiments that mimic the earthquake rupture processes. Our goal was to examine the physical plausibility and conditions under which supershear ruptures can be generated in a controlled laboratory environment. We studied spontaneously nucleated dynamic rupture events in incoherent, frictional interfaces held together by far-field tectonic loads. Thus, we departed from experimental work that addresses the supershear ruptures of coherent interfaces loaded by impact-induced stress waves (15, 16).

An exploding wire-triggering mechanism (Fig. 1C), which simulates a localized pressure release, was used to trigger the rupture (17). This triggering mechanism is inspired by recent numerical work on rupture along frictional interfaces (18, 19). Experimentally, it is a convenient way of triggering the system's full-field, high-speed diagnostics (Fig. 1A) that would otherwise be unable to capture an event with a total duration of  $\sim 50$   $\mu$ s.

More than 50 experiments, featuring a range of angles  $\alpha$  and far-field pressures  $P$ , were performed, and the symmetric bilateral rupture process histories were visualized in intervals of 2  $\mu$ s. Depending on  $P$  and  $\alpha$ , rupture speeds that are either sub-Rayleigh or

supershear were observed. The maximum shear stress field for an experiment with  $\alpha = 25^\circ$  and  $P = 7$  MPa (Fig. 2A) shows that the speed of the rupture tip is very close to  $c_R$  and follows closely behind the circular shear wave front that is emitted at the time of rupture nucleation. The same was found to be true for smaller angles and lower pressures. For an experiment with  $\alpha = 25^\circ$  and  $P = 15$  MPa (Fig. 2B), the circular trace of the shear wave is also visible and is at the same location as in Fig. 2A. However, in front of this circle a supershear disturbance, featuring a Mach cone (pair of shear shock waves), is clearly visible. For this case, the sequences of images before 28  $\mu$ s have a similar form to the image displayed in Fig. 2B and reveal a disturbance that was nucleated as supershear. Its speed history,  $v(t)$ , is determined independently by either the rupture length record or by measuring the angle,  $\beta$ , of the shear shocks with respect to the fault plane and with the use of the relation  $v = c_s/\sin \beta$ . Its speed was 1970 m/s, which is close to the longitudinal wave speed  $c_p$ . In previous experiments involving strong, coherent interfaces and stress wave loading, stable rupture speeds near  $\sqrt{2}c_s$  were observed (15). This apparent discrepancy can be explained by referring to the rupture velocity dependence on the available energy per unit crack advance within the supershear regime (16). This energy attains a maximum value at speeds closer to  $\sqrt{2}c_s$  for strong interfaces. For weaker interfaces, this maximum moves toward  $c_p$ .

To visualize a transition within our field of view (100 mm), we kept  $\alpha = 25^\circ$  but reduced  $P$  to 9 MPa (Fig. 3, A to C). The circular traces of  $P$  and  $S$  waves are visible, followed by a rupture propagating initially at  $c_R$  (Fig. 3A). A small secondary rupture appears in front of the main rupture and propagates slightly ahead of the  $S$  wave front (Fig. 3B). The two ruptures coalesce, and the leading edge of the resulting rupture grows at a speed close to  $c_p$ . The transition length  $L$  here is  $\sim 20$  mm (Fig. 3D).

The above transition phenomenon is comparable with BAM, which is described in (20). Andrews investigated this transition in a parameter space spanned by a normalized supershear transition length,  $L/L_c$ , and a non-dimensional driving stress parameter,  $s$  [ $s =$

<sup>1</sup>Seismological Laboratory, MC 252-21, California Institute of Technology (Caltech), Pasadena, CA 91125, USA. <sup>2</sup>Graduate Aeronautical Laboratories, MC 105-50, Caltech, Pasadena, CA 91125, USA.

\*To whom correspondence should be addressed. E-mail: [hiroo@gps.caltech.edu](mailto:hiroo@gps.caltech.edu)